

# Uncovering origins of heterogeneous superconductivity in $\text{La}_3\text{Ni}_2\text{O}_7$ using quantum sensors

S. V. Mandyam,<sup>1,\*</sup> E. Wang,<sup>1,\*</sup> Z. Wang,<sup>1,\*</sup> B. Chen,<sup>1,\*</sup> N. C. Jayarama,<sup>2</sup> A. Gupta,<sup>1</sup> E. A. Riesel,<sup>3</sup> V. I. Levitas,<sup>4</sup> C. R. Laumann,<sup>1,2,5†</sup> N. Y. Yao<sup>1†</sup>

<sup>1</sup> Department of Physics, Harvard University, Cambridge, MA 02135, USA

<sup>2</sup> Department of Physics, Boston University, Boston, MA 02215, USA

<sup>3</sup> Department of Chemistry, Massachusetts Institute of Technology, Cambridge, Massachusetts 02139, USA

<sup>4</sup> Departments of Aerospace and Mechanical Engineering, Iowa State University, Ames, IA 50011, USA.

<sup>5</sup> Max-Planck-Institut für Physik Komplexer Systeme, 01187 Dresden, Germany

\*These authors contributed equally to this work.

†To whom correspondence should be addressed; E-mail: nyao@fas.harvard.edu; claumann@bu.edu

**The family of nickelate superconductors have long been explored as analogs of the high temperature cuprates [1–6]. Nonetheless, the recent discovery that certain stoichiometric nickelates superconduct up to high  $T_c$  under pressure came as a surprise [7–13]. The mechanisms underlying the superconducting state remain experimentally unclear. In addition to the practical challenges posed by working in a high pressure environment, typical samples exhibit anomalously weak diamagnetic responses, which have been conjectured to reflect inhomogeneous ‘filamentary’ superconducting states [7, 9, 14–17]. We perform wide-field, high-pressure, optically detected magnetic resonance spectroscopy to image the local diamagnetic responses of as grown  $\text{La}_3\text{Ni}_2\text{O}_7$  samples *in situ*, using nitrogen vacancy quantum sensors embedded in the di-**

amond anvil cell [18–21]. These maps confirm significant inhomogeneity of the functional superconducting responses at the few micron scale. By spatially correlating the diamagnetic Meissner response with both the local tensorial stress environment, also imaged *in situ*, and stoichiometric composition, we unravel the dominant mechanisms suppressing and enhancing superconductivity. Our wide-field technique simultaneously provides a broad view of sample behavior and excellent local sensitivity, enabling the rapid construction of multi-parameter phase diagrams from the local structure-function correlations observed at the sub-micron pixel scale.

*Introduction*—Nickelate materials play a crucial role in the decades-long quest to probe, understand and enhance high-temperature (high- $T_c$ ) superconductivity [22–27]. They provide a fresh perspective on the unconventional physics of the cuprates [1–6], realizing similar electronic and structural motifs in a wholly different material platform. For example, the seminal observation of superconductivity in thin-film, square planar nickelates, which are isovalent to the cuprates, hints at a more universal relationship between superconductivity and orbital filling [4, 23, 24, 28–30].

More recently, a tremendous amount of excitement has focused on the discovery of superconductivity in the bulk nickelate,  $\text{La}_3\text{Ni}_2\text{O}_7$ , with a critical temperature above the boiling point of liquid nitrogen [7]. This discovery challenges the nascent paradigm connecting nickelate and cuprate physics:  $\text{La}_3\text{Ni}_2\text{O}_7$  exhibits an electronic configuration that is distinct from the cuprates and only superconducts at high pressures  $\gtrsim 10$  GPa [8–14]. These distinctions suggest the potential to both broaden and deepen our understanding of high- $T_c$  superconductivity. However, realizing this potential comes with its own set of obstacles.

Perhaps the most important, from a practical perspective, is the presence of substantial variations in the superconducting properties measured across different  $\text{La}_3\text{Ni}_2\text{O}_7$  samples [7, 9, 14–

17]. Even when superconductivity is observed, variations exist in the magnitude and sharpness of the drop in resistance, the transition temperature, the local diamagnetic response [31,32], the onset pressure and the characteristics of the normal state [7,14,16]. Moreover, measurements of  $\text{La}_3\text{Ni}_2\text{O}_7$  have also observed strikingly low superconducting volume fractions, leading the superconductivity to be dubbed “filamentary” [10,15]; such observations complicate our understanding of both the nature of nickelate superconductivity, as well as the underlying connection to the cuprates.

Marked progress has been made toward a qualitative understanding of the microscopic origins of the above variations, with invocations to local inhomogeneity in the chemistry [14,33–35], structure [15,36,37], and stress environment [9,10,16]. However, many questions remain. For example, does one of the purported forms of inhomogeneity dominate the superconducting response of  $\text{La}_3\text{Ni}_2\text{O}_7$ ? More quantitatively, is there an interplay between these inhomogeneities and can one identify the associated parameter space hosting superconductivity? The fact that these questions are fundamentally related to the role of local inhomogeneities makes them extremely difficult to answer. Ideally, one would want to spatially correlate the local superconducting properties of  $\text{La}_3\text{Ni}_2\text{O}_7$  with maps of the various types of inhomogeneity. The difficulty of this pursuit is significantly exacerbated by the high-pressure setting, where the *local imaging* of functional material properties remains a perennial challenge.

Here, we take a crucial step toward addressing this challenge: With sub-micron spatial resolution, we directly correlate local regions of superconductivity in  $\text{La}_3\text{Ni}_2\text{O}_7$  with spatial maps of both the stress environment and the chemical composition [Fig. 1]. Our main results are threefold. First, by utilizing diamond anvil cells instrumented with a shallow layer of Nitrogen-Vacancy (NV) color-centers [18–21], we perform wide-field, high-pressure, optically-detected magnetic resonance spectroscopy (ODMR) to image the local diamagnetic response—associated with the superconducting Meissner effect—in three separate  $\text{La}_3\text{Ni}_2\text{O}_7$  samples: S1

[Fig. 2], S2 [Fig. 3] and S3 [Fig. 5]. We note that these samples are carefully chosen to exhibit differing degrees of chemical homogeneity as measured via energy-dispersive X-ray spectroscopy (EDX). Crucially, in addition to NV-based measurements of the diamagnetism, we simultaneously measure the samples’ transport behavior, observing a drop in resistance concomitant with the onset of the Meissner effect [Fig. 2(c,d)]. The proximity of our NV centers to the  $\text{La}_3\text{Ni}_2\text{O}_7$  sample yields excellent magnetic-field sensitivity, which enables the first observation of flux trapping in the nickelates; moreover, we find a direct correlation between those regions of the sample exhibiting diamagnetism and those that trap flux [Fig. 2(e)].

Second, using a complementary modality of the NV sensors, we image the three components of the local stress tensor that define the so-called traction vector:  $\vec{f} = \{\sigma_{XZ}, \sigma_{YZ}, \sigma_{ZZ}\}$  [38]. Crucially,  $\vec{f}$  is continuous across the diamond-sample interface, providing a map of the local stresses experienced by the  $\text{La}_3\text{Ni}_2\text{O}_7$  sample. The traction vector consists of two physically distinct contributions: (i) the normal stress  $\sigma_{ZZ}$  and (ii) the shear stress vector  $\vec{\tau} = \{\sigma_{XZ}, \sigma_{YZ}\}$  with magnitude  $\tau = |\vec{\tau}| = \sqrt{\sigma_{XZ}^2 + \sigma_{YZ}^2}$ , which arises owing to contact friction between the sample and the diamond. Near the critical pressure, we observe the first signatures of superconductivity confined to localized regions of the sample *only* where the normal stress,  $\sigma_{ZZ}$ , is sufficiently large [Fig. 4(b,c)]. Upon further compression, these superconducting regions spread to encompass substantial fractions of the entire sample [Fig. 2(a)]. Perhaps most intriguingly, our spatial maps of the shear stress magnitude,  $\tau$ , yield the following conclusion: above a critical shear of approximately  $\sim 2$  GPa, the superconducting behavior of  $\text{La}_3\text{Ni}_2\text{O}_7$  quenches [Fig. 4(d,e)]. While conventional phase diagrams of nickelate superconductivity depict pressure as a single axis with discrete steps [5, 7, 9, 14, 16, 28], our ability to measure the local stress environment allows us to access a more refined and continuous “pressure” axis [Fig. 4(g,h)]. Indeed, by decomposing this pressure axis into its normal and shear components, we arrive at a complex three-dimensional, superconducting phase diagram for  $\text{La}_3\text{Ni}_2\text{O}_7$  as a function of

$\{T, \sigma_{ZZ}, \tau\}$  [Fig. 4(f)].

Finally, by choosing to work with samples exhibiting noticeable chemical inhomogeneities (S3), we observe the following behavior: local pockets of superconductivity exhibiting sharp diamagnetic transitions even in the absence of an overall drop in sample resistance [Fig. 5(b)]. Crucially, these superconducting pockets overlap with regions of optimal stoichiometry [Fig. 5(e)].

Our experiments are performed on three independent floating-zone-synthesized single crystals (S1, S2, and S3) of  $\text{La}_3\text{Ni}_2\text{O}_7$  [39] mounted within diamond anvil cells (DACs) and connected to transport leads [Fig. 1(b,c)]. The top anvil in each DAC is a type Ib (111)-cut diamond, implanted with a thin layer of NV centers around  $\sim 500$  nm below the culet surface at a density of approximately  $\sim 1$  ppm (Methods) [19, 21]. Each NV center features an  $S = 1$  electronic spin ground state, described by the Hamiltonian  $H_0 = D_{gs}S_Z^2$ , where  $\hat{Z}$  corresponds to the quantization axis along the N-V axis [40, 41]. In the absence of external perturbations, the zero-field splitting,  $D_{gs} = (2\pi) \times 2.87$  GHz, captures the energy difference between the  $|m_s = 0\rangle$  spin sub-level and the two degenerate  $|m_s = \pm 1\rangle$  sub-levels [Fig. 1(d)]; initialization to the  $|m_s = 0\rangle$  state is achieved via optical pumping using a 532 nm laser [42–45].

*NV spectroscopy of local magnetism and stress*—The workhorse of our investigation is the NV’s ability to sense the local magnetic field and stress environment. Both types of perturbations alter the relative energies of the spin sub-levels [Fig. 1(d)]. In particular, magnetic fields  $\vec{B}$  couple through the Zeeman Hamiltonian  $H_B = \gamma \vec{B} \cdot \vec{S}$  [46–49], where  $\gamma$  is the NV spin gyromagnetic ratio, while stress  $\overleftrightarrow{\sigma}$ , which is a rank-2 tensor with six independent elements, couples via the stress Hamiltonian,  $H_\sigma = \Pi_Z S_Z^2 + \Pi_X (S_Y^2 - S_X^2) + \Pi_Y (S_X S_Y + S_Y S_X)$  [18, 50, 51]. Here,  $(\Pi_X, \Pi_Y, \Pi_Z)$  are functions of the stress tensor that transform according to the irreducible representations of the NV point group:  $\Pi_X = -(b + c)(\sigma_{YY} - \sigma_{XX}) + (\sqrt{2}b - \frac{c}{\sqrt{2}})(2\sigma_{XZ})$ ,  $\Pi_Y = -(b + c)(2\sigma_{XY}) + (\sqrt{2}b - \frac{c}{\sqrt{2}})(2\sigma_{YZ})$ , and  $\Pi_Z = (a_1 - a_2)(\sigma_{XX} + \sigma_{YY}) + (a_1 + 2a_2)\sigma_{ZZ}$ , where  $\{a_1, a_2, b, c\}$  correspond to the NV center’s stress susceptibilities (see Methods) [18, 52].

Both magnetic-field- and stress-induced changes to the energies of the NV’s spin sub-levels can be directly read out via optically detected magnetic resonance (ODMR) spectroscopy [40, 53]: owing to differences in the fluorescence of the NV spin sub-levels, a microwave field swept through resonance leads to a characteristic dip in the measured photoluminescence. By imaging this fluorescence onto a CCD, our experiments perform wide-field ODMR spectroscopy and resolve the effects of both perturbations across the entire high-pressure sample chamber (with sub-micron spatial resolution) in a single shot [54, 55].

Two remarks are in order. First, in order to disambiguate the three components of the magnetic field and the six components of the stress tensor, we perform multiple types of measurements on all four sub-groups of NV centers (with different orientations in the diamond lattice, see Methods). Second, owing to both anisotropy and spatial inhomogeneity of the stress environment, the sample does not actually experience a single “pressure”. Our ability to locally resolve the three continuous (across the sample-culet boundary) components of the stress tensor allows us to do better [56]. When it is simplest and most natural to characterize data via a single “pressure”, we will report the averaged normal stress,  $\overline{\sigma_{ZZ}}$ , across the entire sample; this generally agrees quite well with the “pressure” independently measured via the fluorescence wavelength shift of a ruby pellet (see Methods). Otherwise, we will always choose to report the local stress environment, broken down into normal and shear components.

*Transport, Meissner effect and flux trapping in  $\text{La}_3\text{Ni}_2\text{O}_7$* —In order to investigate the local diamagnetic response of  $\text{La}_3\text{Ni}_2\text{O}_7$ , we perform zero-field cooling (ZFC), field warming and field cooling studies (for protocol details, see Methods). In all cases, we apply a uniform external magnetic field,  $H$ , along  $\hat{Z}$ , and then utilize NV centers to measure the local magnetic field,  $B$ , above the sample [Fig. 1(b)]. A diamagnetic sample response, consistent with the superconducting Meissner effect, manifests as a particularly simple expectation: for NVs directly above a diamagnetic region, one expects  $s \equiv \frac{B}{H} < 1$ , corresponding to a local suppression of

the magnetic field; for NVs near the edge of a diamagnetic region, one expects  $s > 1$ , corresponding to the bunching of expelled magnetic field lines; finally, for NVs away from the sample, one simply expects to measure the applied external field and thus  $s \approx 1$  (see Methods for benchmark) [44, 57, 58].

Let us begin by considering the ZFC experimental sequence: At low stresses,  $\overline{\sigma_{ZZ}} \lesssim 15$  GPa, for all three  $\text{La}_3\text{Ni}_2\text{O}_7$  samples, we observe non-superconducting transport behavior and ODMR spectra consistent with  $s = 1$  throughout the entire high-pressure chamber (see Extended Data Fig. 2 and 3). Focusing on S1, as one increases to higher stresses, the NV centers directly above the sample [Fig. 1(b)] begin to exhibit ODMR spectra with  $s \neq 1$ . As an example, Fig. 1(e) shows the ODMR spectra (at  $\overline{\sigma_{ZZ}} = 21$  GPa) obtained along a line-cut that spans the high-pressure chamber. For NVs outside of the sample region (solid white outline, Fig. 1(c)), the ODMR resonances are split by precisely the frequency expected for our external applied field of  $H = 97$  G (yielding  $s \approx 1$ ). For NVs inside the sample region, three distinct types of contiguous ODMR behavior are observed: (i) regions where the ODMR resonances are split by less than expected from the applied field (blue curves, Fig. 1(e), with  $s < 1$ ), (ii) regions where the ODMR resonances are split by more than expected from the applied field (red curves, Fig. 1(e), with  $s > 1$ ), and (iii) regions where the ODMR resonances are consistent with the applied field (gray curves, Fig. 1(e), with  $s \approx 1$ ).

Although we have initially focused on an ODMR line-cut, our wide-field NV microscopy allows us to directly create two-dimensional maps of the local diamagnetic response (as characterized by  $s$ ). Fig. 2(a) illustrates a series of these maps as a function of both normal stress and temperature; here, the temperature values refer to a field warming experiment performed after the previous experimental sequence (i.e. ZFC and then apply  $H$ ), while the normal stress refers to the average of  $\sigma_{ZZ}$  shown in Fig. 2(b). At relatively low normal stresses and high temperatures, one does not observe any signatures of the  $\text{La}_3\text{Ni}_2\text{O}_7$  sample in the maps of  $s$ ,

since  $s \approx 1$  uniformly throughout the high-pressure chamber. At low temperatures and near the optimal normal stress (around  $\overline{\sigma_{ZZ}} = 21$  GPa), we find a pronounced region [blue, Fig. 2(a)] of magnetic-field suppression exhibiting an annular shape; on the left side of this suppression region, we also observe a pronounced region [red, Fig. 2(a)] of magnetic-field enhancement. Both of these features are co-localized with the sample (black dashed line), indicating that they arise from the diamagnetic response of  $\text{La}_3\text{Ni}_2\text{O}_7$ . As one continues to increase the normal stress, two effects are seen: first, the magnitude of the sample's diamagnetic response becomes weaker, and second, the spatial extent of the regions exhibiting this response also decreases [Fig. 2(a)]. Taken together, these data [Fig. 2(a)] evince a particularly elegant visualization of the superconducting dome of  $\text{La}_3\text{Ni}_2\text{O}_7$  in the stress-temperature phase diagram.

More quantitatively, Figure 2(d) presents the magnetic ratio  $s$  as a function of temperature for two specific locations within the sample; one point is chosen to be in a region exhibiting magnetic-field suppression [purple star, bottom right panel of Figure 2(a)], while the other is chosen from a region exhibiting magnetic-field enhancement [pink star, bottom right panel of Figure 2(a)]. For  $\overline{\sigma_{ZZ}} = 21$  GPa, both points exhibit a plateau in  $s$  [at  $s \approx 0.95$  (purple) and  $s \approx 1.05$  (pink)] as the temperature is increased from 20 K to 50 K, before gradually converging to  $s = 1$  at higher temperatures; the temperature at which the two points meet naturally defines a transition temperature of  $T_c \approx 80$  K. Nearly identical behavior is observed for  $\overline{\sigma_{ZZ}} = 25$  GPa, except that the diamagnetism converges to  $s = 1$  at a lower critical temperature,  $T_c \approx 65$  K. Both of these critical temperatures obtained from the sample's diamagnetic response are in perfect agreement with the temperature where the resistance exhibits its first drop [Fig. 2(c)]. This concurrence strongly suggests that the observed local diamagnetism [Fig. 2(a)] originates from the superconducting Meissner effect. To further solidify our findings, we perform the exact same set of measurements on a second sample, S2, as shown in Figure 3. We find analogous behavior both in the local maps of diamagnetism (albeit with a significantly smaller region ex-

hibiting  $s < 1$ ) as a function of stress and temperature [Fig. 3(a)], as well as in the concurrence between transport and diamagnetism [Fig. 3(c)].

Returning to S1, we now leverage the enhanced magnetic-field sensitivity of our proximal NV sensors to directly image flux trapping, for the first time, in  $\text{La}_3\text{Ni}_2\text{O}_7$ . In particular, we cool the sample from room temperature down to 20 K in an applied field of  $H = 150$  G. Then we turn off the magnetic field and perform wide-field ODMR spectroscopy at  $H = 0$  G. Remarkably, as illustrated in Fig. 2(e), many points (in the sample region) exhibit an ODMR spectrum consistent with a remnant magnetic field of up to  $\sim 10$  G. These regions of trapped flux coincide with the regions of Meissner-induced diamagnetism [Fig. 2(e)]; more quantitatively, the regions exhibiting the largest diamagnetic response also trap the largest amount of flux.

*The role of normal and shear stresses*—Our ability to locally determine the sample regions exhibiting a diamagnetic Meissner response opens the door to the following tantalizing possibility: directly identifying the cause of the observed micron-scale spatial variations in superconductivity. Let us begin by exploring the role of the samples’ local stress environment. That there is a superconducting dome in the stress-temperature phase diagram [Fig. 2(a), Fig. 3(a)] immediately yields the following prediction—if there exists substantial heterogeneity in the local normal stress experienced by the sample, then near the phase transition one expects certain regions of the sample to go superconducting first. This simple expectation is indeed borne out by the data. In particular, Fig. 4(c) depicts the local normal stress experienced by sample S1 when  $\overline{\sigma_{ZZ}} = 16$  GPa; we observe marked variations of the normal stress ranging from 13 GPa to 18 GPa, and identify a high-normal-stress region of the sample [dashed black oval, Fig. 4(c)] exhibiting  $\sigma_{ZZ} \gtrsim 17$  GPa. Indeed, the sample begins to exhibit its first signatures of superconductivity in an area that is fully contained within this high-stress region [dashed black oval, Fig. 4(b)]. These observations highlight the limitations intrinsic to assuming a uniform stress environment and attributing superconductivity to a single bulk “pressure”.

Perhaps more importantly, at each temperature, we are able to correlate, pixel by pixel, the sample’s superconducting response,  $s$ , with its local  $\sigma_{ZZ}$ . This has two significant consequences: (i) it essentially renders the stress axis of our superconducting phase diagram *continuous* since every “pressure” point contains a broad distribution of local normal stresses and (ii) it enables a more refined stress-temperature phase diagram where each point in the phase diagram is characterized by a quantitative measure of the sample’s superconducting response,  $s$ . Combining the data across all three samples yields the temperature / normal-stress phase diagram shown in Fig. 4(g), which is in excellent agreement with prior studies [7, 9, 14, 16].

We now turn to data at higher stresses near the optimum. Recall that for sample S1 (at  $\overline{\sigma_{ZZ}} = 21$  GPa), the diamagnetic suppression at the lowest temperatures exhibits a distinct annular shape, with a large region near the center of the sample showing little or no Meissner response [Fig. 4(d)]. One might naturally wonder whether this region is again correlated with spatial variations of the normal stress; we find that this is not the case [see Fig. 2(a)(b)]. Instead, we observe a *striking* correlation between the image of the sample’s diamagnetic response and a map of the local shear stress magnitude  $\tau$  [Fig. 4(e)]. This correlation immediately yields the following conjecture, namely, that superconductivity in  $\text{La}_3\text{Ni}_2\text{O}_7$  is eliminated by the presence of sufficiently large shear stresses. To further explore this conjecture, we again leverage our ability to correlate, pixel by pixel, the sample’s superconducting response with its local shear. In particular, as illustrated in Fig. 4(h), combining the data across all samples, we generate a superconducting phase diagram in the normal-stress / shear-stress plane, uncovering a superconducting dome with a critical shear stress of approximately  $\sim 2$  GPa (see Methods). More generally, the pixel level data allows us to refine the conventional 2D pressure-temperature phase diagram of  $\text{La}_3\text{Ni}_2\text{O}_7$ ’s superconductivity into a 3D phase diagram as a function of temperature, normal stress, and shear stress [Fig. 4(f)].

*The role of chemical composition*—Finally, we investigate the role of local chemical compo-

sition in controlling nickelate superconductivity; indeed, it is well known that multiple distinct Ruddlesden-Popper phases [59], distinguished by different La:Ni stoichiometric ratios, compete during the crystal growth process [24, 25, 39, 60]. Even from the same  $\text{La}_3\text{Ni}_2\text{O}_7$  crystal, we obtain samples exhibiting significant variations in chemical homogeneity as determined via EDX spectroscopy. To this end, we now turn to sample S3, which is chosen specifically for its strong spatial variations in La:Ni stoichiometry. In particular, unlike sample S1 [Fig. 4(a)] and S2 (see Extended Data Fig. 4), which exhibit La:Ni stoichiometries that are relatively homogeneous across the sample, S3 exhibits two pronounced stripe regions with a La:Ni ratio far from the expected optimum of 3:2 [Fig. 5(d)]. This variation in chemistry leads to an immediate impact on the sample’s transport behavior and we do not observe any drop in resistance [top panel, Fig. 5(b)] even near the optimal stress,  $\overline{\sigma_{ZZ}} = 21$  GPa. Nevertheless, at the lowest temperatures ( $T = 9$  K), ODMR spectroscopy (upon ZFC and applying an external field) reveals pockets of weak diamagnetic suppression [Fig. 5(f)]; as before, this suppression vanishes as one increases the temperature above  $T_c \approx 60$  K [bottom panel, Fig. 5(b)]. Overlapping the EDX and ODMR data reveals the following qualitative conclusion—sample regions exhibiting a La:Ni ratio away from 3:2 do not exhibit a diamagnetic response [Fig. 5(e)]. Perhaps a bit more surprisingly, nearly all regions with the correct stoichiometry do seem to exhibit a weak diamagnetic response. More quantitatively, by registering each pixel of the EDX with its associated value of the local superconducting suppression, we demonstrate that a clear optimum in  $s$  emerges at La:Ni = 3:2 [Fig. 5(c)]; this pixel-by-pixel registration also enables the construction of a “stoichiometry-temperature” phase diagram as shown in Extended Data Fig. 4 (see Methods).

*Discussion and conclusion*—Our results are highly significant for both the understanding of nickelate superconductivity, and for high pressure metrology in general. Traditionally, inhomogeneity in samples and sample loadings have rightfully been seen as a significant source of

systematic error in high pressure science and a correspondingly large effort has been expended on achieving homogeneous materials and hydrostatic pressure environments [61, 62]. With the ability to locally image both functional material properties and the tensorial stress environment, one may instead view a single inhomogeneous sample as a collection of many micron-scale samples that can be simultaneously characterized to construct multi-parameter phase diagrams. Rather than a source of error to be mitigated, inhomogeneity becomes a resource to be mined. Indeed, this perspective lies behind our selection of the particular  $\text{La}_3\text{Ni}_2\text{O}_7$  samples that were measured, and enabled our observation of the role of *shear* in suppressing and eliminating the superconducting state; we note that this complements recent observations of the importance of *in-plane stress* in epitaxially-strained thin films [60, 63].

Our work opens the door to a number of intriguing future directions. First, our magnetic maps show regions of *paramagnetic* response which turn on below  $T_c$  (e.g. Fig. 2(a)). Such a response is naturally expected from the compression of magnetic field lines near the boundary of superconducting regions in the Meissner state. However, we find that the paramagnetic regions are not necessarily proximate to diamagnetic regions, which suggests the possibility of an alternative mechanism at work. One such possibility is the so-called Wohlleben effect first observed in granular cuprate superconductors, and taken as early indirect evidence for exotic pairing symmetry [64–67]. Second, while our approach has identified several mechanisms underlying the heterogeneity of  $\text{La}_3\text{Ni}_2\text{O}_7$  superconductivity, much variability remains to be explained (e.g. sample S2). Frequently invoked mechanisms which might play an important role include oxygen doping [33–35, 63, 68] and layer stacking variations [36, 37]. These and other conjectured mechanisms may be confirmed by correlating NV-DAC magnetic functional responses with a growing range of structural and compositional imaging techniques such as nanoscale secondary ion mass spectrometry [69] and micron resolution synchrotron X-ray diffraction [70]. Third, understanding the microscopic mechanism by which shear stress de-

stroys superconductivity in  $\text{La}_3\text{Ni}_2\text{O}_7$  is an intriguing open question. Example potential mechanisms include plastic deformations or a shear distortion of the angle of the Ni-O bond, which controls the coupling between bilayers. Finally, zooming out a bit, we note that many state-of-the-art computational methods use experimentally measured fields to help determine the tensorial stress and plastic strain inside a material [71, 72]. Direct experimental access to the traction field,  $\vec{f}$ , at the diamond-sample boundary could significantly augment the capabilities of such numerical methods. In the context of  $\text{La}_3\text{Ni}_2\text{O}_7$ , it would be interesting to apply such methods to determine *all* of the tensorial fields in the sample and to further extend our understanding of the role of stress on nickelate superconductivity.

*Acknowledgments*—We very gratefully acknowledge Meng Wang and Mengwu Huo for providing the nickelate samples used in this study. We also acknowledge Gengda Gu for supplying the BSCCO samples used for benchmarking. We thank the Fischer lab for generous access to their high pressure sample preparation equipment. We thank Timothy Cavanaugh, Stephan Kraemer, and Shao-Liang Zheng for their assistance using shared facilities. These include the Harvard University Center for Nanoscale Systems (CNS), a member of the National Nanotechnology Coordinated Infrastructure Network (NNCI), supported by the National Science Foundation under NSF award no. ECCS-2025158, and the X-Ray Core facility, supported by the Major Research Instrumentation (MRI) NSF award no. 2216066. This work is supported by the Brown Institute for Basic Sciences. S. V. M. acknowledges support from the National Science Foundation Graduate Research Fellowship under Grant No. DGE-1752814. V. I. L. acknowledges support of the NSF (DMR-2246991), ARO (W911NF2420145) and Iowa State University (Murray Harpole Chair in Engineering). C. R. L. is grateful for support through a Martin Gutzwiller Fellowship at MPIPKS, where his work was in part supported by the Deutsche Forschungsgemeinschaft under Grant No. SFB 1143 (Project-Id 247310070) and the cluster of excellence ct.qmat (EXC 2147, Project-Id 390858490). N.Y.Y. acknowledges support

from a Simons Investigator award.

*Author Contributions*— S. V. M., E. W., Z. W. and B. C. prepared samples, performed experiments and data analysis. S. V. M., Z. W., A. G., and B. C. developed the analysis software. S. V. M., Z. W., and N. C. J. worked on theoretical models and simulated the effect of stress on the NV center, with guidance from V. I. L., C. R. L. and N. Y. Y.. S. V. M., E. W., Z. W. and E. A. R. calibrated the diamond miscut. C. R. L. and N. Y. Y. proposed and interpreted investigations of sample, and supervised the project. S. V. M., E. W., Z. W., B. C., N. C. J., C. R. L., and N. Y. Y. wrote the manuscript with input from all authors.

*Competing interests*— Harvard University (co-inventors S. V. M., E. W., Z. W., B. C., N. C. J., C. R. L., N. Y. Y.) filed for a provisional patent that relates to wide-field imaging of the stress tensor under pressure using spin defects embedded in a diamond anvil cell.

*Data availability*— Published data are available on the Zenodo public database.

## References

- [1] Anisimov, V., Bukhvalov, D. & Rice, T. Electronic structure of possible nickelate analogs to the cuprates. *Physical Review B* **59**, 7901 (1999).
- [2] Lee, K.-W. & Pickett, W. Infinite-layer lanio 2: Ni 1+ is not cu 2+. *Physical Review B—Condensed Matter and Materials Physics* **70**, 165109 (2004).
- [3] Botana, A. S. & Norman, M. R. Similarities and differences between lanio 2 and cacuo 2 and implications for superconductivity. *Physical Review X* **10**, 011024 (2020).
- [4] Goodge, B. H. *et al.* Doping evolution of the mott-hubbard landscape in infinite-layer nickelates. *Proceedings of the National Academy of Sciences* **118**, e2007683118 (2021).

- [5] Wú, W., Luo, Z., Yao, D.-X. & Wang, M. Superexchange and charge transfer in the nickelate superconductor  $\text{La}_3\text{Ni}_2\text{O}_7$  under pressure. *Science China Physics, Mechanics & Astronomy* **67**, 117402 (2024). URL <https://doi.org/10.1007/s11433-023-2300-4>.
- [6] Yang, J. *et al.* Orbital-dependent electron correlation in double-layer nickelate  $\text{La}_3\text{Ni}_2\text{O}_7$ . *Nature Communications* **15**, 4373 (2024). URL <https://www.nature.com/articles/s41467-024-48701-7>.
- [7] Sun, H. *et al.* Signatures of superconductivity near 80 K in a nickelate under high pressure. *Nature* **621**, 493–498 (2023). URL <https://www.nature.com/articles/s41586-023-06408-7>.
- [8] Chen, X. *et al.* Electronic and magnetic excitations in  $\text{La}_3\text{Ni}_2\text{O}_7$ . *Nature Communications* **15**, 1–9 (2024). URL <https://www.nature.com/articles/s41467-024-53863-5>.
- [9] Li, J. *et al.* Identification of Superconductivity in Bilayer Nickelate  $\text{La}_3\text{Ni}_2\text{O}_7$  under High Pressure up to 100 GPa. *National Science Review* nwaf220 (2025). URL <https://doi.org/10.1093/nsr/nwaf220>.
- [10] Wang, G. *et al.* Pressure-induced superconductivity in polycrystalline  $\text{La}_3\text{Ni}_2\text{O}_7$ . *Physical Review X* **14**, 011040 (2024).
- [11] Schlömer, H., Schollwöck, U., Grusdt, F. & Bohrdt, A. Superconductivity in the pressurized nickelate  $\text{La}_3\text{Ni}_2\text{O}_7$  in the vicinity of a BEC–BCS crossover. *Communications Physics* **7**, 1–8 (2024). URL <https://www.nature.com/articles/s42005-024-01854-9>.

[12] Geisler, B., Hamlin, J. J., Stewart, G. R., Hennig, R. G. & Hirschfeld, P. J. Structural transitions, octahedral rotations, and electronic properties of  $\text{A3Ni2O7}$  rare-earth nickelates under high pressure. *npj Quantum Materials* **9**, 1–9 (2024). URL <https://www.nature.com/articles/s41535-024-00648-0>.

[13] Dan, Z. *et al.* Spin-density-wave transition in double-layer nickelate  $\text{La3Ni2O7}$  (2024). URL <http://arxiv.org/abs/2402.03952>.

[14] Zhang, Y. *et al.* High-temperature superconductivity with zero resistance and strange-metal behaviour in  $\text{La3Ni2O7-}\delta$ . *Nature Physics* **20**, 1269–1273 (2024). URL <https://www.nature.com/articles/s41567-024-02515-y>.

[15] Zhou, Y. *et al.* Investigations of key issues on the reproducibility of high- $\text{tc}$  superconductivity emerging from compressed  $\text{La3Ni2O7}$ . *Matter and Radiation at Extremes* **10** (2025).

[16] Hou, J. *et al.* Emergence of High-Temperature Superconducting Phase in Pressurized  $\text{La3Ni2O7}$  Crystals. *Chinese Physics Letters* **40**, 117302 (2023). URL <https://doi.org/10.1088/0256-307X/40/11/117302>.

[17] Shi, M. *et al.* Prerequisite of superconductivity: SDW rather than tetragonal structure in double-layer  $\text{La3Ni2O7-x}$  (2025). URL <http://arxiv.org/abs/2501.14202>.

[18] Hsieh, S. *et al.* Imaging stress and magnetism at high pressures using a nanoscale quantum sensor. *Science* **366**, 1349–1354 (2019). URL <https://www.science.org/doi/10.1126/science.aaw4352>.

[19] Lesik, M. *et al.* Magnetic measurements on micrometer-sized samples under high pressure using designed nv centers. *Science* **366**, 1359–1362 (2019).

[20] Yip, K. Y. *et al.* Measuring magnetic field texture in correlated electron systems under extreme conditions. *Science* **366**, 1355–1359 (2019).

[21] Bhattacharyya, P. *et al.* Imaging the meissner effect in hydride superconductors using quantum sensors. *Nature* **627**, 73–79 (2024).

[22] Wang, B. Y., Lee, K. & Goodge, B. H. Experimental progress in superconducting nickelates. *Annual Review of Condensed Matter Physics* **15** (2024).

[23] Li, D. *et al.* Superconductivity in an infinite-layer nickelate. *Nature* **572**, 624–627 (2019).

[24] Pan, G. A. *et al.* Superconductivity in a quintuple-layer square-planar nickelate. *Nature materials* **21**, 160–164 (2022).

[25] Ko, E. K. *et al.* Signatures of ambient pressure superconductivity in thin film La<sub>3</sub>Ni<sub>2</sub>O<sub>7</sub>. *Nature* **638**, 935–940 (2025). URL <https://www.nature.com/articles/s41586-024-08525-3>. Publisher: Nature Publishing Group.

[26] Mitchell, J. F. A Nickelate Renaissance. *Frontiers in Physics* **9** (2021). URL <https://www.frontiersin.org/articles/10.3389/fphy.2021.813483>.

[27] Nomura, Y. & Arita, R. Superconductivity in infinite-layer nickelates. *Reports on Progress in Physics* **85**, 052501 (2022). URL <https://dx.doi.org/10.1088/1361-6633/ac5a60>.

[28] Zeng, S. *et al.* Superconductivity in infinite-layer nickelate la<sub>1-x</sub>ca<sub>x</sub>ni<sub>2</sub> thin films. *Science advances* **8**, eabl9927 (2022).

[29] Wang, B. Y. *et al.* Isotropic Pauli-limited superconductivity in the infinite-layer nickelate Nd<sub>0.775</sub>Sr<sub>0.225</sub>NiO<sub>2</sub>. *Nature Physics* **17**, 473–477 (2021). URL <https://www.nature.com/articles/s41567-020-01128-5>.

[30] Hu, K. *et al.* Atomic scale disorder and reconstruction in bulk infinite-layer nickelates lacking superconductivity. *Nature Communications* **15**, 5104 (2024). URL <https://www.nature.com/articles/s41467-024-49533-1>.

[31] Liu, L. *et al.* Evidence for the Meissner Effect in the Nickelate Superconductor  $\text{La}_3\text{Ni}_2\text{O}_7$  Single Crystal Using Diamond Quantum Sensors. *Physical Review Letters* **135**, 096001 (2025). URL <https://link.aps.org/doi/10.1103/PhysRevLett.135.096001>. Publisher: American Physical Society.

[32] Wen, J. *et al.* Imaging the meissner effect in pressurized bilayer nickelate with integrated multi-parameter quantum sensor. *National Science Review* (2025). URL <http://dx.doi.org/10.1093/nsr/nwaf268>.

[33] Dong, Z. *et al.* Visualization of oxygen vacancies and self-doped ligand holes in  $\text{La}_3\text{Ni}_2\text{O}_7-\delta$ . *Nature* **630**, 847–852 (2024).

[34] Chen, Y. *et al.* Oxygen deficiency mechanism of  $\text{La}_3\text{Ni}_2\text{O}_7-\delta$  under pressure. *Science China Physics, Mechanics & Astronomy* **68**, 247411 (2025). URL <https://doi.org/10.1007/s11433-024-2556-4>.

[35] Sui, X. *et al.* Formation of unusual oxygen vacancy chains in nickelate  $\text{La}_3\text{Ni}_2\text{O}_7$ . *Physical Review B* **110**, 205125 (2024). URL <https://link.aps.org/doi/10.1103/PhysRevB.110.205125>.

[36] Puphal, P. *et al.* Unconventional crystal structure of the high-pressure superconductor  $\text{La}_3\text{Ni}_2\text{O}_7$ . *Physical Review Letters* **133**, 146002 (2024).

[37] Chen, X. *et al.* Polymorphism in the ruddlesden–popper nickelate  $\text{La}_3\text{Ni}_2\text{O}_7$ : discovery of a hidden phase with distinctive layer stacking. *Journal of the American Chemical Society* **146**, 3640–3645 (2024).

[38] Reddy, J. N. *An introduction to continuum mechanics* (Cambridge university press, 2013).

[39] Liu, Z. *et al.* Evidence for charge and spin density waves in single crystals of  $\text{La}_3\text{Ni}_2\text{O}_7$  and  $\text{La}_3\text{Ni}_2\text{O}_6$ . *Science China Physics, Mechanics & Astronomy* **66**, 217411 (2022). URL <https://doi.org/10.1007/s11433-022-1962-4>.

[40] Schirhagl, R., Chang, K., Loretz, M. & Degen, C. L. Nitrogen-vacancy centers in diamond: nanoscale sensors for physics and biology. *Annual review of physical chemistry* **65**, 83–105 (2014).

[41] Doherty, M. W. *et al.* The nitrogen-vacancy colour centre in diamond. *Physics Reports* **528**, 1–45 (2013). URL <https://www.sciencedirect.com/science/article/pii/S0370157313000562>.

[42] Wickenbrock, A. *et al.* Microwave-free magnetometry with nitrogen-vacancy centers in diamond. *Applied Physics Letters* **109**, 053505 (2016). URL <https://doi.org/10.1063/1.4960171>.

[43] Kuwahata, A. *et al.* Magnetometer with nitrogen-vacancy center in a bulk diamond for detecting magnetic nanoparticles in biomedical applications. *Scientific Reports* **10**, 2483 (2020). URL <https://www.nature.com/articles/s41598-020-59064-6>.

[44] Joshi, K. *et al.* Measuring the Lower Critical Field of Superconductors Using Nitrogen-Vacancy Centers in Diamond Optical Magnetometry. *Physical Review Applied* **11**, 014035 (2019). URL <https://link.aps.org/doi/10.1103/PhysRevApplied.11.014035>.

[45] Mittiga, T. *et al.* Imaging the Local Charge Environment of Nitrogen-Vacancy Centers in Diamond. *Physical Review Letters* **121**, 246402 (2018). URL <https://link.aps.org/doi/10.1103/PhysRevLett.121.246402>.

[46] Tsukamoto, M. *et al.* Vector magnetometry using perfectly aligned nitrogen-vacancy center ensemble in diamond. *Applied Physics Letters* **118**, 264002 (2021). URL <https://doi.org/10.1063/5.0054809>.

[47] Scheidegger, P. J., Diesch, S., Palm, M. L. & Degen, C. L. Scanning nitrogen-vacancy magnetometry down to 350 mK. *Applied Physics Letters* **120**, 224001 (2022). URL <https://doi.org/10.1063/5.0093548>.

[48] Casola, F., van der Sar, T. & Yacoby, A. Probing condensed matter physics with magnetometry based on nitrogen-vacancy centres in diamond. *Nature Reviews Materials* **3**, 1–13 (2018). URL <https://www.nature.com/articles/natrevmats201788>.

[49] Dai, J.-H. *et al.* Optically Detected Magnetic Resonance of Diamond Nitrogen-Vacancy Centers under Megabar Pressures. *Chinese Physics Letters* **39**, 117601 (2022). URL <https://dx.doi.org/10.1088/0256-307X/39/11/117601>.

[50] Hilberer, A. *et al.* Enabling quantum sensing under extreme pressure: Nitrogen-vacancy magnetometry up to 130 GPa. *Physical Review B* **107**, L220102 (2023). URL <https://link.aps.org/doi/10.1103/PhysRevB.107.L220102>.

[51] Udvarhelyi, P., Shkolnikov, V. O., Gali, A., Burkard, G. & Pályi, A. Spin-strain interaction in nitrogen-vacancy centers in diamond. *Physical Review B* **98**, 075201 (2018). URL <https://link.aps.org/doi/10.1103/PhysRevB.98.075201>.

[52] Maze, J. R. *et al.* Properties of nitrogen-vacancy centers in diamond: the group theoretic approach. *New Journal of Physics* **13**, 025025 (2011). URL <https://iopscience.iop.org/article/10.1088/1367-2630/13/2/025025>.

[53] Broadway, D. *et al.* Improved Current Density and Magnetization Reconstruction Through Vector Magnetic Field Measurements. *Physical Review Applied* **14**, 024076 (2020). URL <https://link.aps.org/doi/10.1103/PhysRevApplied.14.024076>.

[54] Scholten, S. C. *et al.* Widefield quantum microscopy with nitrogen-vacancy centers in diamond: Strengths, limitations, and prospects. *Journal of Applied Physics* **130**, 150902 (2021). URL <https://doi.org/10.1063/5.0066733>.

[55] Scholten, S. C. *et al.* Aberration control in quantitative widefield quantum microscopy. *AVS Quantum Science* **4**, 034404 (2022). URL <http://arxiv.org/abs/2207.12675>.

[56] Landau, L. D. *Theory of Elasticity: By L.D. Landau and E.M. Lifshitz. Translated from the Russian by J.B. Sykes and W.H. Reid* (Pergamon Press, 1964). Google-Books-ID: 3rFQswEACAAJ.

[57] Schlussel, Y. *et al.* Wide-Field Imaging of Superconductor Vortices with Electron Spins in Diamond. *Physical Review Applied* **10**, 034032 (2018). URL <https://link.aps.org/doi/10.1103/PhysRevApplied.10.034032>.

[58] Thiel, L. *et al.* Quantitative nanoscale vortex imaging using a cryogenic quantum magnetometer. *Nature Nanotechnology* **11**, 677–681 (2016). URL <https://www.nature.com/articles/nnano.2016.63>. Publisher: Nature Publishing Group.

[59] Ruddlesden, S. & Popper, P. New compounds of the  $\text{k}_2\text{ni}\text{f}_4$  type. *Acta Crystallographica* **10**, 538–539 (1957).

[60] Bhatt, L. *et al.* Resolving structural origins for superconductivity in strain-engineered  $\text{La}_3\text{Ni}_2\text{O}_7$  thin films. *arXiv preprint arXiv:2501.08204* (2025).

[61] Klotz, S., Chervin, J.-C., Munsch, P. & Le Marchand, G. Hydrostatic limits of 11 pressure transmitting media. *Journal of Physics D: Applied Physics* **42**, 075413 (2009). URL <https://iopscience.iop.org/article/10.1088/0022-3727/42/7/075413>.

[62] Tempere, J. & Silvera, I. F. Pressure distribution in a quasi-hydrostatic pressure medium: A finite element analysis. *Journal of Applied Physics* **110**, 113523 (2011). URL <https://pubs.aip.org/jap/article/110/11/113523/147740/Pressure-distribution-in-a-quasi-hydrostatic>.

[63] Wang, B. Y. *et al.* Electronic structure of compressively strained thin film  $\text{La}_2\text{PrNi}_2\text{O}_7$ . *arXiv preprint arXiv:2504.16372* (2025).

[64] da Silva, R. M., Milošević, M. V., Shanenko, A. A., Peeters, F. M. & Aguiar, J. A. Giant paramagnetic Meissner effect in multiband superconductors. *Scientific Reports* **5**, 12695 (2015). URL <https://www.nature.com/articles/srep12695>.

[65] Parhizgar, F. & Black-Schaffer, A. M. Diamagnetic and paramagnetic Meissner effect from odd-frequency pairing in multiorbital superconductors. *Physical Review B* **104**, 054507 (2021). URL <https://link.aps.org/doi/10.1103/PhysRevB.104.054507>.

[66] Geim, A. K., Dubonos, S. V., Lok, J. G. S., Henini, M. & Maan, J. C. Paramagnetic Meissner effect in small superconductors. *Nature* **396**, 144–146 (1998). URL <https://www.nature.com/articles/24110>.

[67] Braunisch, W. *et al.* Paramagnetic Meissner effect in high-temperature superconductors. *Physical Review B* **48**, 4030–4042 (1993). URL <https://link.aps.org/doi/10.1103/PhysRevB.48.4030>. Publisher: American Physical Society.

[68] Shen, J. *et al.* Anomalous energy gap in superconducting  $\text{La}_{0.75}\text{Pr}_{0.15}\text{Ni}_2\text{O}_4$  heterostructures. *arXiv preprint arXiv:2502.17831* (2025).

[69] Li, K., Liu, J., Grovenor, C. R. M. & Moore, K. L. NanoSIMS Imaging and Analysis in Materials Science. *Annual Review of Analytical Chemistry* **13**, 273–292 (2020). URL <https://www.annualreviews.org/content/journals/10.1146/annurev-anchem-092019-032524>. Publisher: Annual Reviews.

[70] MacDowell, A. A. *et al.* Submicron X-ray diffraction. *Nuclear Instruments and Methods in Physics Research Section A: Accelerators, Spectrometers, Detectors and Associated Equipment* **467-468**, 936–943 (2001). URL <https://www.sciencedirect.com/science/article/pii/S0168900201005307>.

[71] Levitas, V. I., Dhar, A. & Pandey, K. Tensorial stress-plastic strain fields in  $\alpha$ - $\omega$  Zr mixture, transformation kinetics, and friction in diamond-anvil cell. *Nature Communications* **14**, 5955 (2023).

[72] Dhar, A. *et al.* Quantitative kinetic rules for plastic strain-induced  $\alpha$  -  $\omega$  phase transformation in Zr under high pressure. *npj Computational Materials* **10**, 1–13 (2024). URL <https://www.nature.com/articles/s41524-024-01491-4>.

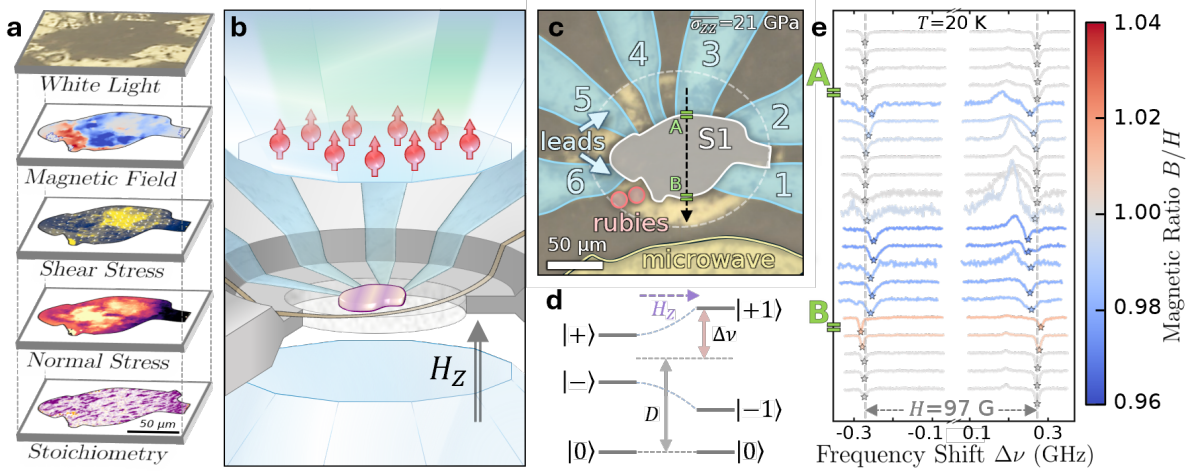


**Fig. 1: Micron-scale structure-function mapping at high pressure in an NV-DAC.** **a** The Nitrogen-Vacancy equipped Diamond Anvil Cell (NV-DAC) enables submicron-scale imaging of functional magnetic responses of samples at high pressure. Correlating these maps with the local stress environment (from *in situ* NV-DAC tensor barometry) and local chemical composition (eg. from EDX) permits a wealth of structure-function information to be obtained from a single inhomogenous sample. **b** Schematic depiction of the sample loading between two opposing anvils. The top anvil contains a layer of NV centers approximately 500 nm below the culet surface. A platinum wire for microwave delivery and leads for electronic transport measurements are placed on the insulated gasket, facing the top diamond. We note that there is a  $\sim 3^\circ$  misalignment between the culet normal and the [111] NV symmetry axis, which is discussed in the Methods. **c** White light image of sample S1 with false color overlays obtained at 21 GPa. A crystal of  $\text{La}_3\text{Ni}_2\text{O}_7$  (gray) is embedded in NaCl as a pressure medium (tan) within an insulating cBN gasket (dark). **d** Schematic of the spin  $S = 1$  sub-levels of the electronic ground state of the NV center. The common shift  $D = D_{gs} + \Pi_Z(\overleftrightarrow{\sigma})$  of the upper two levels depends on the stress tensor  $\overleftrightarrow{\sigma}$  but is insensitive to the magnetic field. The splitting  $\Delta\nu$  is dominated by the linear Zeeman effect due to the magnetic field  $B_z$  along the NV axis. The positions of peaks in the optically-detected magnetic resonance (ODMR) spectra (e) thus reflect the local magnetic and stress fields. **e** The ODMR spectra obtained at regularly spaced pixels along the line cut indicated after zero-field cooling (ZFC) to temperature 20 K and turning on a magnetic field of  $H = 97$  G. Away from the sample boundaries (points A and B), the measured splitting  $\Delta\nu \approx 0.27$  GHz is consistent with a local  $B = 97$  G, while above the sample there are regions where  $\Delta\nu$  is both smaller (magnetic suppression) and larger (enhancement) than normal state expectations. Spectra are scaled to have uniform peak contrast, but are otherwise unprocessed. We observe inverted ‘positive contrast’ peaks, which extend our ability to measure both magnetic fields and traction to higher pressures (see Methods for details).

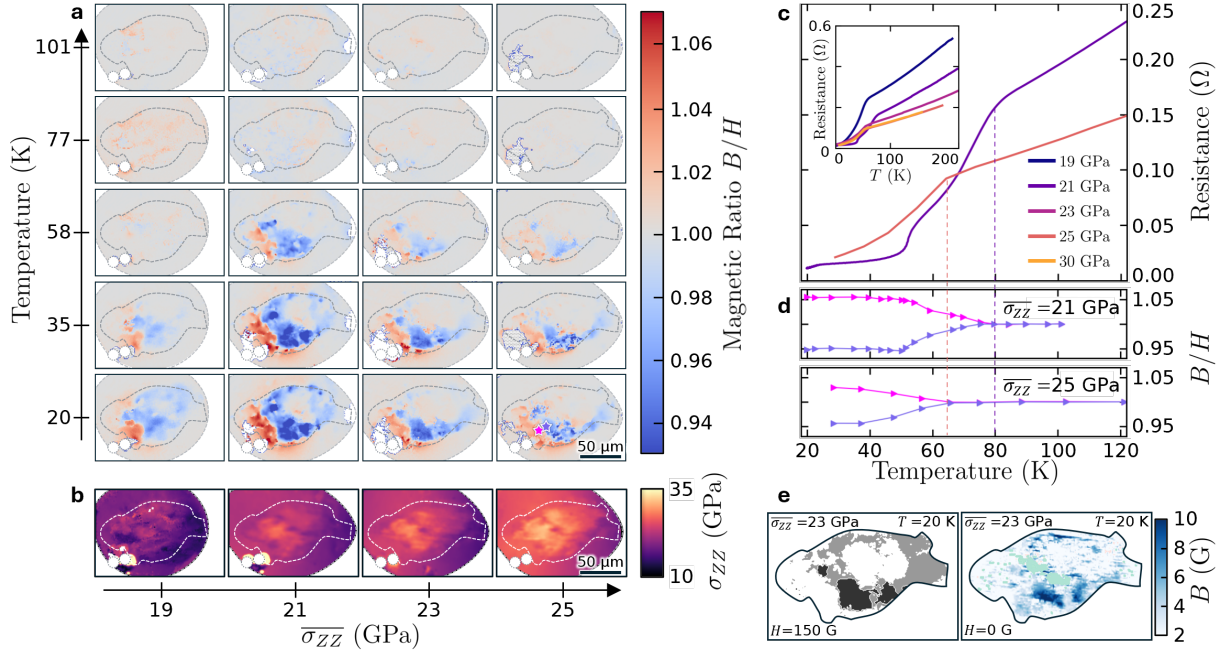


**Fig. 2: Imaging local superconductivity and flux trapping.** **a** Sub-micron diffraction-limited maps of sample S1, showing the magnetic field  $B$  obtained after zero-field cooling (ZFC) to 20 K, turning on  $H \sim 100$  G and then field warming (FW). The magnetic ratio  $s \equiv B/H$  above the sample deviates from 1 below a dome in the  $\sigma_{ZZ}, T$  plane, although clear spatial inhomogeneities exist. **b** Corresponding  $\sigma_{ZZ}$  maps for these stress points, taken at 150 K. **c**, **d** Simultaneously measured resistance at  $\sigma_{ZZ} = 21$  and 25 GPa, with the ZFC-FW magnetic response of two spatial points marked on (a) [pink and purple stars, bottom right panel]. Kinks in the magnetic response correspond to kinks in resistance at corresponding stress points. **e** Spatial regions of strongest ZFC diamagnetic response (left) at  $\sigma_{ZZ} = 23$  GPa correspond to regions with the most remnant magnetic flux (right) trapped after field cooling (FC) at  $H = 150$  G and quenching to  $H = 0$  G. For the left panel, gray regions correspond to  $0.97 \leq B/H < 1$  while black regions correspond to  $0.85 \leq B/H < 0.97$ . For the right panel, green regions correspond to ODMR spectra with NV resonances that were unable to be resolved.

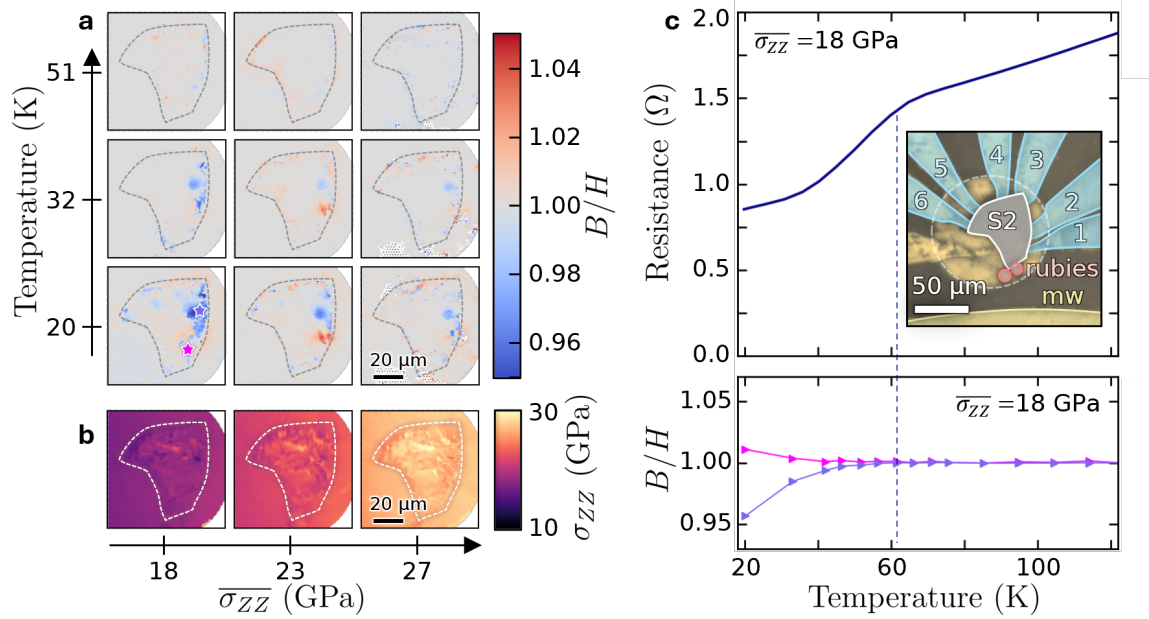


**Fig. 3: Local superconductivity and normal stress maps.** **a** Maps of the ZFC-FW magnetic response and **b** normal stress maps of sample S2 analogous to those in Fig. 2 for sample S1. **c** Correlation of the resistive transition (above) with the magnetic response (below) at one stress point. Sample S2 shows qualitatively similar diamagnetic and resistive responses to those of sample S1 in the  $\bar{\sigma}_{ZZ} - T$  plane but in a smaller spatial volume and with a weaker local  $s$  response.

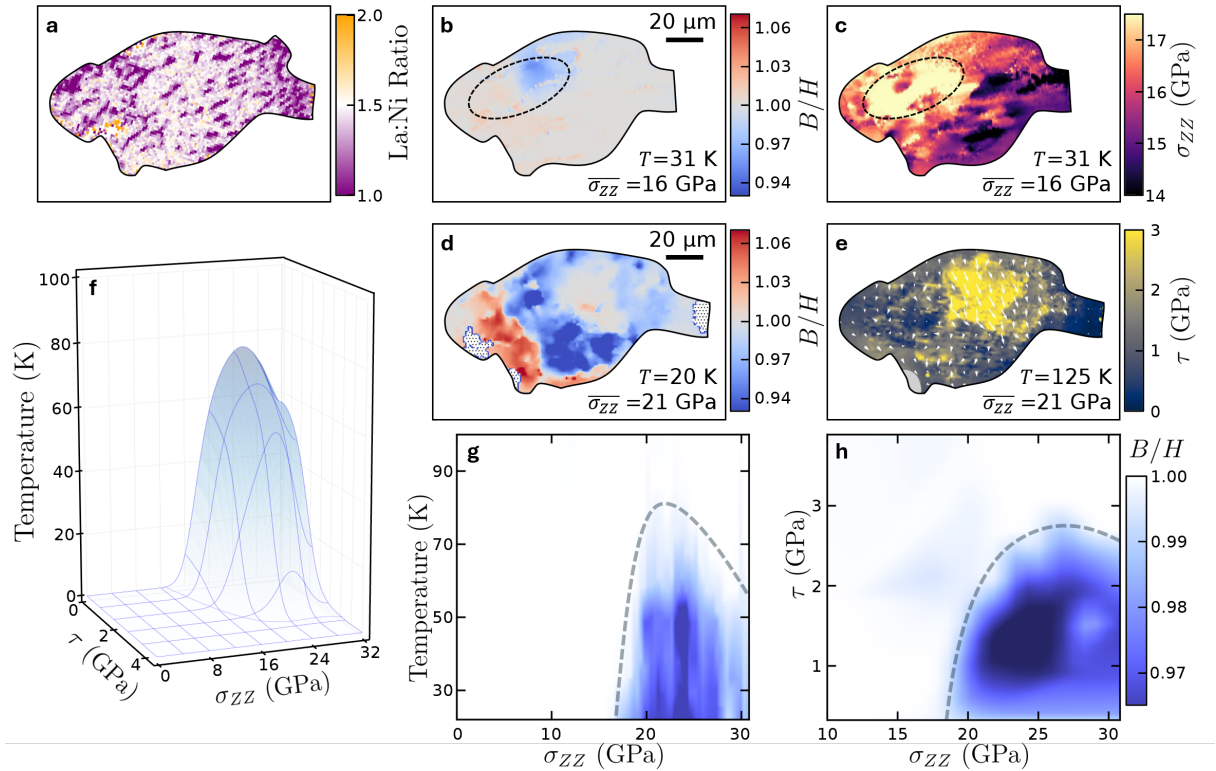


**Fig. 4: Multimodal correlations, superconducting phase diagram and the role of shear stresses.** **a** The local surface stoichiometry of sample S1 obtained via energy-dispersive X-ray spectroscopy (EDX) shows regular Ni rich inclusions (purple) at the several micron scale as well as smaller regions of enhanced La (orange). This chemical texture does not alone explain the bulk features observed in the ZFC magnetic response. For example, at the lowest stress point,  $\overline{\sigma_{ZZ}} = 16$  GPa, where S1 exhibits diamagnetic response **b**, the region of the sample that goes superconducting turns out to be locally at higher normal stress  $\sigma_{ZZ} \approx 17.5$  GPa than the mean shown in panel **c**. **e** The shear stress vector  $\tau$  with components  $(\sigma_{XZ}, \sigma_{YZ})$  (white arrows) across the culet boundary at optimal mean stress,  $\overline{\sigma_{ZZ}} = 21$  GPa. Color indicates the magnitude of the shear stress vector  $\tau$ . The region of high shear correlates strongly with the hole in the annular region of diamagnetic response in the corresponding ZFC-FW magnetic response shown in panel **d**. Gray region indicates overlap with ruby pellet which prevents the accurate extraction of the local shear. **f** depicts a three dimensional phase diagram of the superconducting response as a function of temperature, normal stress, and shear stress. Data is extrapolated down to zero on all axes using a spline fit (see Methods). Note that there is no data extrapolation for the phase diagrams shown in the subsequent panels (g) and (h). **g** The superconducting dome in the temperature, normal stress plane extracted from pixel-registered local responses across samples S1-S3. Dashed line corresponds to a guide to the eye delineating the superconducting region. **h** A low temperature projection of the phase diagram in the normal and shear stress plane. The dashed line provides a guide to the eye delineating the superconducting region.

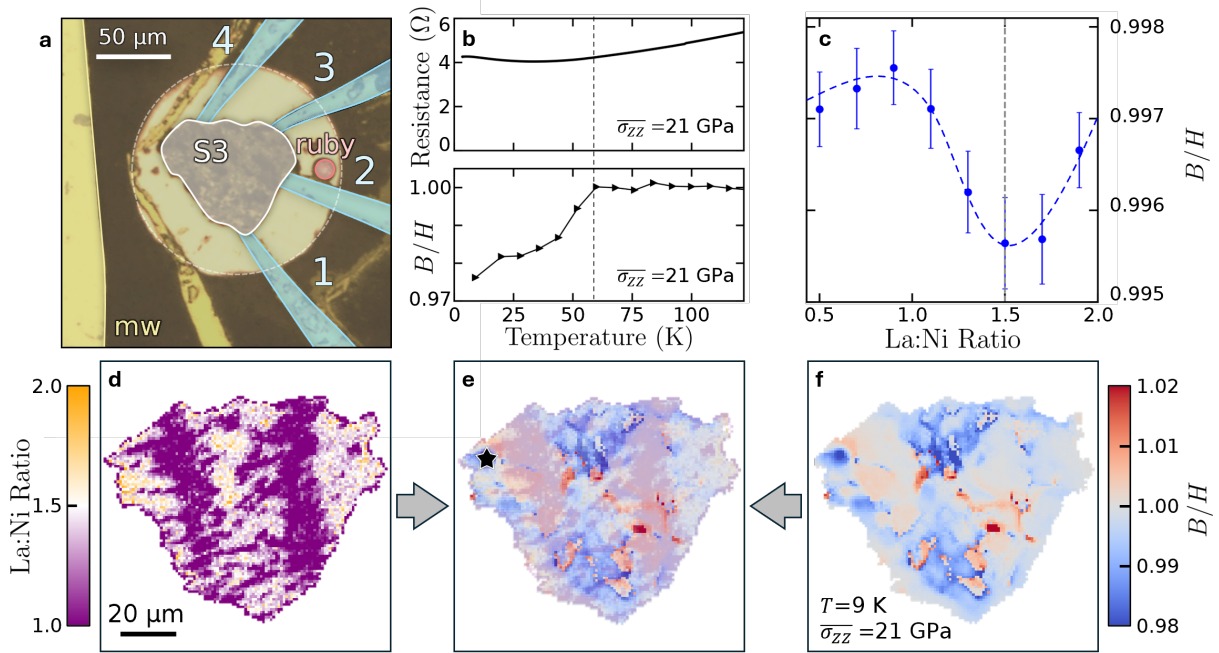


**Fig. 5: Correlating local superconductivity with chemistry.** **a** Optical image of S3 (gray) with transport leads (blue), microwave antenna (yellow) and ruby (red). **b** Global four terminal resistance (above) shows no visible kinks even as the local diamagnetic response (black star in (e)) turns on below 60K (below). **c** The local ZFC diamagnetic response ( $B/H$ ) at 9 K shows a sharp peak where the ratio of La:Ni obtained by EDX is in the expected 3:2 ratio of stoichiometric  $\text{La}_3\text{Ni}_2\text{O}_7$ . The dashed line serves as a guide to the eye. **d** The spatial map of the La:Ni ratio shows two large stripes of enhanced Ni which cut across S3. These correlate strongly with regions which fail to show a magnetic response when overlaid (panel **e**) with the magnetic map obtained after ZFC at 9 K as shown in panel **f**.